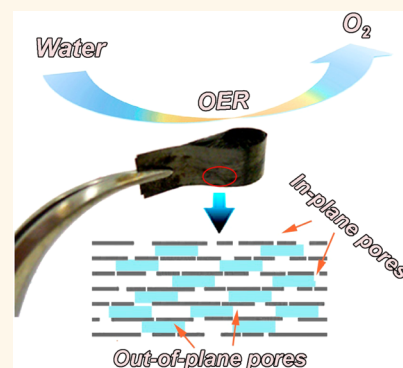


# Hierarchically Porous Nitrogen-Doped Graphene–NiCo<sub>2</sub>O<sub>4</sub> Hybrid Paper as an Advanced Electrocatalytic Water-Splitting Material

Sheng Chen and Shi-Zhang Qiao\*

School of Chemical Engineering, University of Adelaide, Adelaide, SA5005, Australia

**ABSTRACT** In this work, we report a three-dimensional (3D) oxygen evolution reaction (OER) catalyst with hierarchical pores for water splitting. The remarkable features of well-developed in- and out-of-plane pores, 3D conductive networks, and N-doping have greatly promoted the transport in electrodes and assured high catalytic efficiency. The 3D hybrid paper of N-doped graphene–NiCo<sub>2</sub>O<sub>4</sub> has shown a remarkable OER catalytic activity that was comparable to that of previously reported noble metal catalysts (IrO<sub>2</sub>). The catalytic process occurred with favorable kinetics and strong durability. The dual-active-site mechanism is responsible for the excellent performance of the hybrid catalyst; that is, the edges of NiCo<sub>2</sub>O<sub>4</sub> and the N (O)–metal (Ni or Co) bonds are both active sites. This study affords a new strategy to achieve optimal performance in 3D catalysts, which may be extended to the preparation of other 3D hybrid materials for a broad range of technological applications.



**KEYWORDS:** hierarchical porous structure · nitrogen-doped graphene · ternary metal oxides · oxygen evolution · synergistic effect

Catalysts are critical elements in many important technological processes.<sup>1,2</sup> Recently, there has been an intensive effort to investigate the use of nanomaterials with three-dimensional (3D) architectures as advanced catalysts for a number of key renewable energy systems.<sup>3,4</sup> These studies include integration of MoS<sub>x</sub> into nickel foam for hydrogen generation<sup>3</sup> and porous carbon coated on nickel foam for oxygen evolution.<sup>4</sup> The great interest in 3D catalysts is probably promoted by the recognition that 3D architectures could significantly enhance catalytic activity and kinetics due to their high catalyst loadings and excellent catalyst–electrode contact. Note that nickel foam was exclusively used to prepare 3D catalysts, probably due to its low price, high conductivity, and rich macroporosity. However, problems with nickel foam could be the difficulties in tailoring its properties and structures, such as pore structures. As the porosity directly determines the transport in catalytic processes, the capability of manipulating pores is crucial for achieving optimal performances

for 3D catalysts. As a consequence, the study of a new class of 3D catalysts with tunable pores and properties is emerging. Recently, graphene-based 3D macrostructures, such as self-supported films, have received extensive interest due to their exceptional electrical and mechanical properties.<sup>5–7</sup> Interestingly, the properties and microstructures of graphene can be rationally tuned through various chemical methods. For example, their electron-donor properties were tailored by doping graphene sheets with other elements such as nitrogen (N), which has increased the catalytic activities.<sup>8,9</sup> Also, two kinds of pores, *i.e.*, out-of-plane and in-plane, have been introduced into graphene sheets, which have led to enhanced kinetics.<sup>10–14</sup> Out-of-plane pores generated by adding “spacers” between graphene sheets can improve the mass transport,<sup>10</sup> while in-plane pores are usually created by techniques such as copolymer lithography,<sup>11</sup> enzymatic oxidation,<sup>12</sup> and chemical activation,<sup>13,14</sup> which have shortened the diffusion path lengths and expanded electrode–electrolyte contact areas.

\* Address correspondence to s.qiao@adelaide.edu.au.

Received for review August 26, 2013 and accepted October 3, 2013.

Published online October 03, 2013  
10.1021/nn404444r

© 2013 American Chemical Society

In this aspect, self-supported graphene films would be very suitable candidates for developing a new generation of 3D catalysts. By blending N-doping with in- and out-of-plane pores, the resulting hierarchically porous N-doped graphene films should feature both high activity and favorable kinetics.

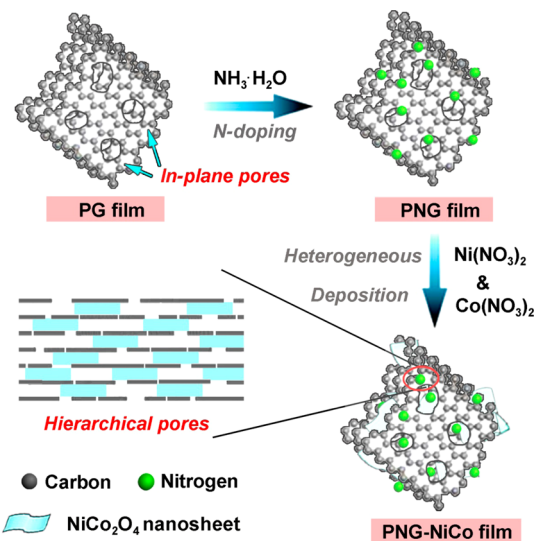
Meanwhile, the oxygen evolution reaction (OER), which is the bottleneck of the water-splitting process, is naturally sluggish and usually proceeds on noble metal catalysts such as  $\text{IrO}_2$  and  $\text{RuO}_2$ .<sup>15–19</sup> In view of their prohibitive price and scarcity, various low-cost alternatives, such as  $\text{NiCo}_2\text{O}_4$ , have been developed.<sup>15–17,20–23</sup> Efforts for enhancing the performances of  $\text{NiCo}_2\text{O}_4$  mainly include tailoring its microstructures or using nanostructured supports.<sup>22–24</sup> Despite the great interest in various carbonaceous supports such as graphene sheets, there are no reports of using 3D N-doped porous graphene films for the controllable assembly of  $\text{NiCo}_2\text{O}_4$ . Such hybrid systems are attractive targets, as they permit the use of advanced properties of both materials, such as high activity of  $\text{NiCo}_2\text{O}_4$ , rich porosity, 3D conductive network, and excellent mechanical properties of porous graphene films along with the strong N–metal bonding.

Herein, we report an advanced 3D structured catalyst fabricated on the basis of N-doped graphene films with in- and out-of-plane pores. The key of this study is the use of in-plane porous graphene as precursors and to generate the out-of-plane pores by adding  $\text{NiCo}_2\text{O}_4$  between graphene sheets, which can substantially improve the catalytic processes occurring in the electrode. By taking advantage of its advanced structural properties, the 3D hybrid film of porous N-doped graphene– $\text{NiCo}_2\text{O}_4$  (denoted as PNG-NiCo) showed a remarkable catalytic activity toward OER, which was comparable to that of previously reported noble metal catalysts.<sup>18,19</sup> The enhanced performance is correlated with the dual-active-site mechanisms originating from the synergistic effects of graphene and  $\text{NiCo}_2\text{O}_4$ . The 3D catalyst paper is obtained in a highly flexible and macroscopic form; thus it can be easily further processed and integrated into various devices.

## RESULTS AND DISCUSSION

The synthesis of 3D hybrid catalysts is described in Scheme 1. First, graphene was oxidized and etched with  $\text{KMnO}_4$  and hydrochloric acid (HCl) to create in-plane pores on the sheet, which was then filtrated into a self-supported film (porous graphene film, or PG). Next, N atoms were doped onto graphene sheets by using ammonia to generate the N-doped porous graphene film (PNG). Subsequently, the PNG-NiCo hybrid was achieved *via* a heterogeneous reaction process by heating the PNG film in a mixed solution containing  $\text{Ni}(\text{NO}_3)_2$  and  $\text{Co}(\text{NO}_3)_2$  (see Methods section for details).

PNNG-NiCo is a highly flexible macroscopic film of a few centimeters in size and only  $\sim 17 \mu\text{m}$  in thickness



**Scheme 1.** Fabrication of 3D hybrid catalyst (note: PG, PNG, and PNG-NiCo signify porous graphene, porous N-doped graphene, and porous N-doped graphene– $\text{NiCo}_2\text{O}_4$  hybrid, respectively).

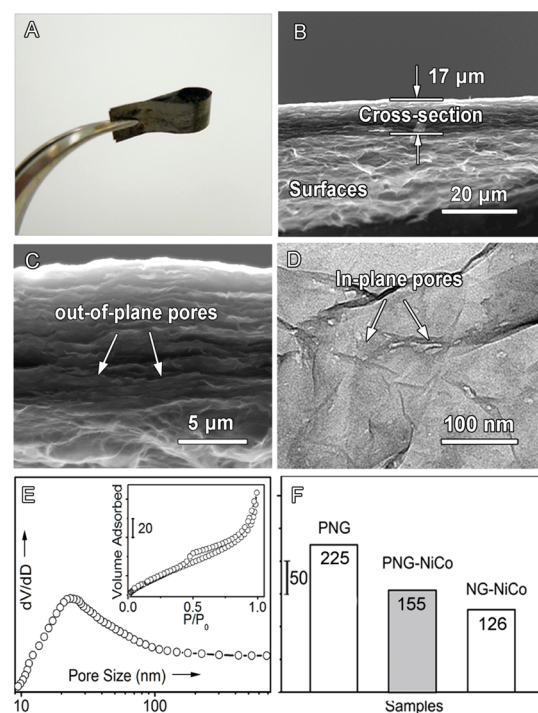


**Figure 1.** (A) Optical image and (B, C) SEM images of PNG-NiCo; (D) TEM image of PNG; (E) pore size distribution (expressed in  $\text{cm}^3 \text{g}^{-1} \text{nm}^{-1}$ ) of PNG-NiCo; the inset in (E) shows the corresponding nitrogen adsorption–desorption isotherm (expressed in  $\text{cm}^3 \text{STP g}^{-1}$ ) for PNG-NiCo; (F) specific surface area (expressed in  $\text{m}^2 \text{g}^{-1}$ ) of PNG, PNG-NiCo, and NG-NiCo measured by methylene blue (MB) experiments.

(Figure 1A,B). The large out-of-plane macropores afforded by a relatively oriented assembly of graphene sheets in PNG-NiCo range from tens of nanometers to a few micrometers (scanning electron microscopy, SEM, Figure 1C). The relatively ordered lamellar structure of

PNG-NiCo is different from many previously reported graphene architectures formed by randomly aggregated sheets, such as graphene hydrogels and aerogels,<sup>25,26</sup> which may promote effective transport in the catalytic process. Moreover, the in-plane pores of PNG-NiCo observed by transmission electron microscopy (TEM, Figure 1D) are small mesopores in the range of several to tens of nanometers randomly distributed on graphene sheets. The observation of both out-of-plane macropores and in-plane mesopores in PNG-NiCo is consistent with its nitrogen adsorption analyses, where the adsorption isotherm resembles type IV with an obvious capillary condensation step (hysteresis loop) (Figure 1E).<sup>27,28</sup> The corresponding pore size distribution obtained by the Barrett–Joyner–Halenda (BJH) method shows the presence of mesopores and small macropores ranging from 10 to 100 nm. Note that  $\text{NiCo}_2\text{O}_4$  and PNG-NiCo have a similar pore size distribution (Figure S1B), but the pores of  $\text{NiCo}_2\text{O}_4$  stem from the restacking of nanoparticles, which is different from those of PNG-NiCo, stemming from both in-plane pores of graphene sheets and restacking pores of  $\text{NiCo}_2\text{O}_4$ . The nitrogen adsorption of  $\text{NiCo}_2\text{O}_4$  only accounts for 7.1% of the adsorbed amount of PNG-NiCo at a relative pressure of  $P/P_0 \approx 1.0$  (9 vs 126  $\text{cm}^3 \text{STP g}^{-1}$ ), thus indicating that porous graphene is the main contributor of nitrogen adsorption of PNG-NiCo. Further, the high surface area of PNG-NiCo was also proved by a methylene blue (MB) adsorption experiment (155  $\text{m}^2 \text{g}^{-1}$ , Figures 1F,S2).<sup>29,30</sup> The surface area of PNG-NiCo estimated from the MB absorption experiment exceeds that of its counterpart (N-doped graphene– $\text{NiCo}_2\text{O}_4$  film or NG-NiCo) with only out-of-plane pores (155 vs 126  $\text{m}^2 \text{g}^{-1}$ ), underlining the importance of hierarchical pores for achieving highly accessible surfaces for catalysts.

SEM and TEM images further confirm that PNG-NiCo is composed of graphene and  $\text{NiCo}_2\text{O}_4$ , where two discrepant structures are clearly observed, *i.e.*, the almost transparent graphene sheet and a thick  $\text{NiCo}_2\text{O}_4$  sheet uniformly coated on graphene (Figure 2A,B). A control experiment shows that  $\text{NiCo}_2\text{O}_4$  grown on nickel foam forms nanosheets a few nanometers thick and a few micrometers in size (Figure S3). HRTEM images of PNG-NiCo show the (440) crystal lattice of  $\text{NiCo}_2\text{O}_4$  inside the hybrid material (Figure S4A,B). The element mapping shows homogeneous C, N, Co, and Ni distributions inside PNG-NiCo (Figure S4C). Carbon atoms originate from the framework of graphene, N atoms from the N-doping of graphene using ammonia, and Co and Ni atoms from  $\text{NiCo}_2\text{O}_4$ . The presence of  $\text{NiCo}_2\text{O}_4$  in the hybrid is also supported by the X-ray diffraction (XRD, Figure 2C), in which almost all the prominent peaks of PNG-NiCo match well with cubic phase  $\text{NiCo}_2\text{O}_4$  (JPCDS card no. 20-0781). Moreover, graphene and  $\text{NiCo}_2\text{O}_4$  account for 34.1 wt % and 65.9 wt % of PNG-NiCo, respectively, as determined

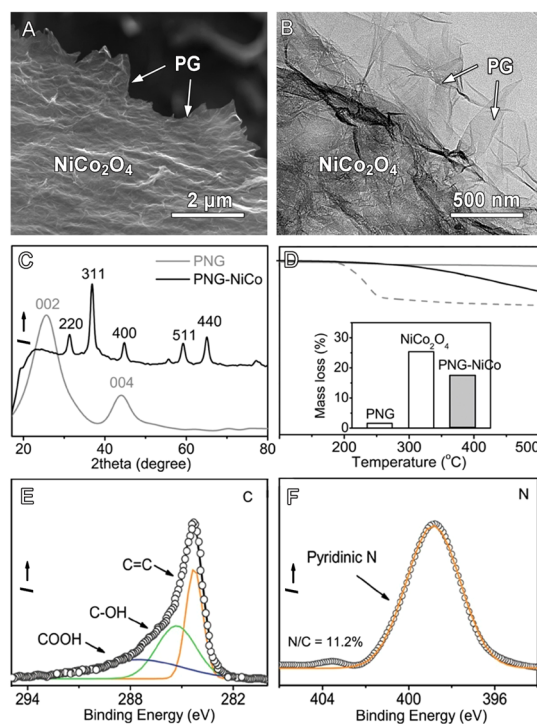


**Figure 2.** (A) SEM and (B) TEM images of PNG-NiCo; (C) XRD patterns of PNG-NiCo and PNG; (D) TGA plots of PNG-NiCo, PNG, and  $\text{NiCo}_2\text{O}_4$ ; the inset in (D) is the mass loss of the corresponding samples; high-resolution XPS C1s (E) and N1s (F) spectra of PNG-NiCo.

by thermal gravimetric analysis (TGA, Figure 2D). X-ray photoelectron spectroscopy (XPS) and energy-dispersive X-ray spectroscopy (EDS) suggest PNG-NiCo contains C, O, N, Ni, and Co as the main elements (Figure S5A,B). The high-resolution C1 XPS spectrum signifies a number of functional groups on graphene sheets, such as hydroxyl (C–OH) and carboxyl (–COOH) groups (Figure 2E), which might interact with  $\text{NiCo}_2\text{O}_4$  by covalent chemical bonding, hydrogen bonding, or van der Waal's forces and enable the direct growth of  $\text{NiCo}_2\text{O}_4$  on graphene sheets. The N/C ratio in PNG-NiCo is ~11.2%, with the pyridinic N structure dominating on the graphene sheets (Figure 2F). The functional groups of hydroxyl (C–OH) or carboxyl (–COOH) as well as pyridinic N atoms in PNG-NiCo may provide additional active sites for the catalytic process.

The OER catalytic properties were investigated in a three-electrode system directly using PNG-NiCo as a working electrode. PNG-NiCo shows a high activity with the small onset potential of 310 mV (linear scan voltammograms, LSV, Figure 3A), which is more negative than other samples such as NG-NiCo (340 mV), PNG (352 mV), and porous graphene– $\text{NiCo}_2\text{O}_4$  hybrid films (PG-NiCo, 315 mV, Figure S6A). The high activity was also demonstrated by comparing the current density of PNG-NiCo with others, showing that PNG-NiCo explicitly outperforms others over the whole potential range. Note that the catalytic current of PNG-NiCo reaches 5  $\text{mA cm}^{-2}$  at the overpotential of 373 mV;

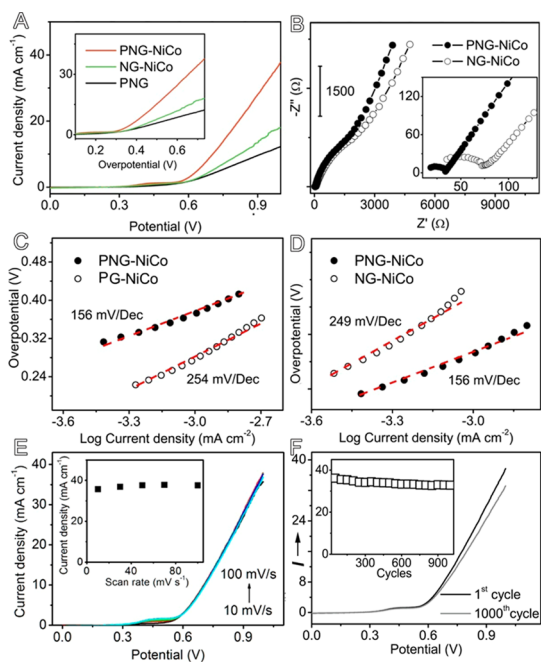


**Figure 3.** (A) LSV plots of PNG-NiCo, NG-NiCo, and PNG at  $50 \text{ mV s}^{-1}$  in  $0.1 \text{ M KOH}$ ; the inset in (A) shows the corresponding data replotted as the current density vs overpotential; (B) EIS spectra of PNG-NiCo and NG-NiCo; Tafel plots for PNG-NiCo in comparison to those for PG-NiCo (C) and NG-NiCo (D), respectively; (E) LSV plots of PNG-NiCo at different scan rates; the inset in (E) shows the corresponding data replotted as the current density (at  $1.0 \text{ V vs Ag/AgCl}$ ) vs scan rates; (F) LSV plots for PNG-NiCo (express as  $\text{mA cm}^{-2}$ ) before and after CV testing of 1000 cycles; the inset of (F) shows the relationship between current density (expressed as  $\text{mA cm}^{-2}$ , at  $1.0 \text{ V vs Ag/AgCl}$ ) and cycle numbers.

when the overpotential is  $564 \text{ mV}$ , the OER current density of PNG-NiCo is  $21.1 \text{ mA cm}^{-2}$ . These values are even comparable to that of previously reported noble-metal catalysts.<sup>18,19</sup> Further, the performance of our catalyst was compared with previously reported  $\text{NiCo}_2\text{O}_4$  samples. As expected, our material shows better performance than many others; for example, it has a smaller overpotential than nickel cobalt nanowire arrays ( $310 \text{ vs } 379 \text{ mV}$ ).<sup>23</sup> Moreover, when the overpotential is  $434 \text{ mV}$  ( $700 \text{ mV vs Ag/AgCl}$ ), it has a higher current density of  $16.5 \text{ mA cm}^{-2}$  than  $\text{NiCo}_2\text{O}_4$  obtained by the propionic acid sol–gel route ( $10 \text{ mA cm}^{-2}$ ) and  $\text{NiCo}_2\text{O}_4$  prepared by dip-coating and sequential solution coating ( $9.33 \text{ mA cm}^{-2}$ ).<sup>22</sup>

On the other hand, the catalytic kinetics of PNG-NiCo was examined with a number of characterizations. Electrical impedance spectroscopy (EIS, Figures 3B, S7), performed on PNG-NiCo, NG-NiCo, and PG-NiCo, respectively, is composed of two regions, *i.e.*, a semi-circle at high frequencies and a linear part at low frequencies. As compared to NG-NiCo and PG-NiCo, PNG-NiCo has a low charge transfer resistance ( $12.2 \Omega$  for PNG-NiCo vs  $23.8 \Omega$  for NG-NiCo and  $27.6 \Omega$  for PG-NiCo, obtained from the x-axis intercept of semicircle), corresponding to favorable charge transport kinetics.

Note that PNG-NiCo and PG-NiCo have similar precipitous slopes in the linear part of the EIS, indicating similar mass transport properties within the electrodes (Figure S7). Moreover, Tafel plots of the samples are recorded with the linear regions fitted into the Tafel equation ( $\eta = b \log j + a$ , where  $\eta$  is the overpotential,  $j$  is the current density, and  $b$  is the Tafel slope, Figures 3C,D and S6B). The enhanced kinetics of PNG-NiCo is also approved by its lower Tafel slope of  $156 \text{ mV dec}^{-1}$  than other samples such as NG-NiCo ( $249 \text{ mV dec}^{-1}$ ), PG-NiCo ( $254 \text{ mV dec}^{-1}$ ), and PNG ( $168 \text{ mV dec}^{-1}$ ). Meanwhile, we note that PNG-NiCo and PG-NiCo only slightly change their catalytic currents with increasing scan rates from  $10$  to  $100 \text{ mV s}^{-1}$  ( $<5\%$ , Figures 3E, S5A), probably due to their hierarchical pores that allow efficient charge and mass transport in catalytic process. While in the case of NG-NiCo with only out-of-plane pores, the transport process might be insufficient, as evidenced by significant current increase under a similar testing condition (20.4%, Figure S8). This result has provided additional support for the critical role of hierarchical porosity for efficient catalysis.

Furthermore, the high stability of catalysts toward OER is important for energy conversion systems. PNG-NiCo showed excellent durability in alkaline electrolyte with less than 10% anodic current loss during  $\sim 1000$  continuous potential cyclings (cyclic voltammetry, CV, Figure 3F). Also, the chronoamperometric test of PNG-NiCo demonstrated only slight current attenuation (less than 10%) after operation for  $10 \text{ h}$  (Figure S9). The remarkable features of high activity, favorable kinetics, and strong durability suggest PNG-NiCo is a promising candidate to catalyze OER for water splitting.

The enhanced performance of PNG-NiCo is associated with its advanced structural properties. First, the hierarchical pores of PNG-NiCo can enhance the transport during catalytic processes for favorable kinetics (Figures 3B–D and S6B). Specifically, its large out-of-plane pores (macropores, Figure 1C) can facilitate the mass transport and infiltration of electrolytes, while the small in-planes pores (mesopores, Figure 1D) can provide high surface area and short diffusion path lengths. The hierarchical porosity of PNG-NiCo was also confirmed by both nitrogen adsorption and MB experiments (Figures 1E,F and S2), and the enhanced kinetics were proved by its low charge transfer resistance (Figure 3B), small Tafel slope (Figures 3C,D and S6B), and insignificant current change with increasing scan rates (Figure 3E). Second, the use of 3D graphene architecture for controllable assembly of  $\text{NiCo}_2\text{O}_4$  significantly contributes to enhanced activity (Figures 3A, S6A). FTIR of PNG-NiCo (Figure 4A) shows features of both graphene ( $-\text{COOH}$ ,  $\text{C}-\text{O}(\text{N})$ ) and  $\text{NiCo}_2\text{O}_4$  ( $\text{Ni}-\text{O}$  and  $\text{Co}-\text{O}$ ). The functional groups of graphene in PNG-NiCo have played dual roles, *i.e.*, interacting with water molecules to render the hybrid film somewhat

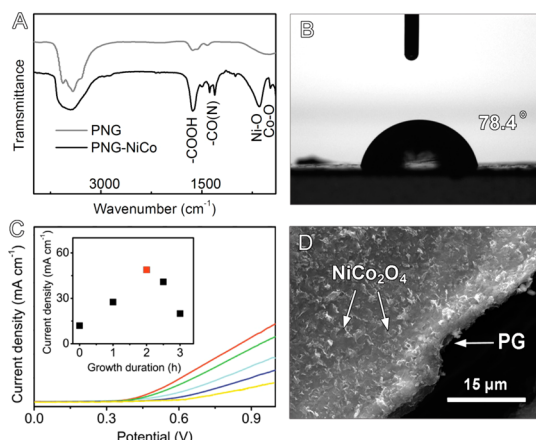


**Figure 4.** (A) FTIR spectra of PNG-NiCo and PNG; (B) contact angle of PNG-NiCo; (C) LSV plots of PNG-NiCo with different growth duration of  $\text{NiCo}_2\text{O}_4$ ; the insets in (C) show the relationship of current density (at 1 V vs Ag/AgCl) vs growth duration; (D) SEM image of PNG-NiCo with the growth duration of 3 h.

hydrophilic for more accessible catalytic surfaces (Figure 4B) and simultaneously acting as anchoring sites to bridge  $\text{NiCo}_2\text{O}_4$  and graphene. The contact angle of PNG-NiCo is similar to that of PNG (78.4° vs 76.7°) due to the presence of similar functional groups in these samples (Figures 4A, S10A). Note that PNG-NiCo shows a smaller contact angle than pristine graphite (78.4° vs 90.3°, Figure S10B) because the former is more hydrophilic than the latter. Control experiments show the growth duration of  $\text{NiCo}_2\text{O}_4$  is a critical factor to achieve an optimal performance for hybrid catalysts (Figure 4C,D). The direct growth of  $\text{NiCo}_2\text{O}_4$  on graphene films with 3D conductive networks can impart the effective charge transport in electrodes, which can maximize the use of  $\text{NiCo}_2\text{O}_4$  for high activity. Further, the 3D catalyst exhibited excellent electrochemical stability toward OER presumably due to its unique layer-by-layer structure. In the common nickel foam-based electrodes, active species are decorated on the surface of scaffolds, and they are vulnerable to peeling off from substrates during a long-term cycling. In contrast,  $\text{NiCo}_2\text{O}_4$  in the PNG-NiCo paper can be fully accommodated between graphene sheets in the macroscopic film, where

their volume change during the catalytic process can be effectively buffered by adjacent graphene sheets with excellent mechanical properties to afford high durability.

The mechanism of hybrid catalyst has been discussed on the basis of literature and experimental results.  $\text{NiCo}_2\text{O}_4$ , as a typical 3D transition-metal oxide, is particularly active for catalyzing OER because it can interact with water molecules to form  $\text{Ni}(\text{Co})-\text{O}$  bonding and consequently expedite the catalytic process.<sup>31,32</sup> Similar to other transition-metal catalysts,<sup>16,24</sup> the edges and defective sites of  $\text{NiCo}_2\text{O}_4$  are the active centers to facilitate the dissociation of water. Meanwhile, the strong interactions between  $\text{NiCo}_2\text{O}_4$  and N-doped graphene afforded by direct growth of  $\text{NiCo}_2\text{O}_4$  on graphene sheets have also contributed to enhanced OER activity. In view of the relatively low electronegativity of O or N atoms of N-doped graphene, they might interact with  $\text{NiCo}_2\text{O}_4$  to form strong O (N)–metal (Ni, Co) bonds.<sup>24</sup> Therefore, besides  $\text{NiCo}_2\text{O}_4$ , the strong interactions of O (N)–metal (Ni, Co) are the other active centers for expediting water dissociation. Because the activity of PNG without  $\text{NiCo}_2\text{O}_4$  only accounts for 31.5% of PNG-NiCo,  $\text{NiCo}_2\text{O}_4$  should be the main active species in the hybrid.

## CONCLUSIONS

In conclusion, we have proposed the first design and synthesis of a hierarchically porous N-doped graphene– $\text{NiCo}_2\text{O}_4$  film as an advanced OER catalyst. The resulting material combines a number of remarkable features such as well-developed in- and out-of-plane pores, a 3D conductive network, and excellent mechanical flexibility. This novel material has exhibited significantly enhanced catalytic performances with high catalytic activity, favorable kinetics, and strong durability. Further, the dual-active-site mechanism is proposed for the 3D catalyst, which may afford rich active centers in the catalytic process. The materials are prepared through a facile strategy that is expected to be further promoted to prepare a wide range of other 3D architectures for various applications such as metal–air batteries, solar cells, and photocatalysis.

## METHODS

**Synthesis.** Graphite oxide (GO) was prepared from natural graphite *via* Hummers' method<sup>33</sup> and was exfoliated by ultrasonication using a Brandson digital sonifier (S450D, 500 W, 30% amplitude) for ~30 min. Next, in-plane pores of graphene were introduced by oxidizing and etching GO with  $\text{KMnO}_4$  and HCl. Specifically, the GO dispersion (100 mL, ~0.5 mg mL<sup>-1</sup>) was mixed with potassium permanganate ( $\text{KMnO}_4$ , 500 mg) in a covered beaker for 2 h. The above solution was merged with 30 mL of HCl and 30 mL of hydrogen peroxide ( $\text{H}_2\text{O}_2$ ) for 3 h. The product, *i.e.*, porous graphene oxide or PGO, was collected and washed with deionized (DI) water. The concentration of

as-prepared PGO was determined by comparing its ultraviolet–visible spectra (UV–vis) absorbance to that of a GO solution with known concentration.

The porous graphene film (denoted as PG) was prepared through a filtration method. Specifically, PGO (200 mL, 0.1 mg mL<sup>-1</sup>) was first mixed with a small amount of ammonia (0.8 mL) and hydrazine hydrate (0.08 mL) followed by heating at 95 °C for 12 h. Most of the functional groups of PGO were removed except carboxyl (–COOH),<sup>34</sup> which can be ionized into –COO<sup>–</sup> in alkaline solution to make graphene sheets highly negatively charged (zeta potential –50.5 mV, Figure S11). The electrostatic repulsion then can prevent the aggregation of graphene sheets

and enable the formation of a well-dispersed black aqueous dispersion (inset in Figure S11). Next, the as-obtained porous graphene dispersion was filtered through a mixed cellulose ester filter membrane (0.05  $\mu\text{m}$  pore size). When the solution was just drained out, the vacuum suction was stopped. The resultant filtration cake was immediately transferred to a Petri dish and dialyzed for 12 h.

Next, the PG film was doped with nitrogen (N) atoms by adding ammonia ( $\text{NH}_3 \cdot \text{H}_2\text{O}$ , 30 mL ~35 wt % in water) and heating at 150  $^{\circ}\text{C}$  for 12 h. The as-obtained N-doped PG film (denoted as PNG) was dialyzed against DI water for 12 h.

The hybrid film of N-doped porous graphene– $\text{NiCo}_2\text{O}_4$  (denoted as PNG-NiCo) was prepared through a heterogeneous reaction method. Specifically, 1 mmol of  $\text{Ni}(\text{NO}_3)_2 \cdot 6\text{H}_2\text{O}$ , 2 mmol of  $\text{Co}(\text{NO}_3)_2 \cdot 6\text{H}_2\text{O}$ , and 12 mmol of urea were dissolved into a mixed solution of ethanol (20 mL) and  $\text{H}_2\text{O}$  (20 mL), generating the intermediate complex  $[\text{M}(\text{H}_2\text{O})_{6-x}(\text{urea})_x]^{2+}$ . Then the PNG film was mixed with the above solution and heated at 90  $^{\circ}\text{C}$  for 2 h. The metal complex  $[\text{M}(\text{H}_2\text{O})_{6-x}(\text{urea})_x]^{2+}$  began to decompose into metal oxide nuclei ( $\text{NiCo}_2\text{O}_4$ ). During this process, the functional groups of graphene, such as  $-\text{COOH}$ , can act as anchor sites to interact with metal oxide nuclei through hydrogen bonding, van der Waals forces, or covalent interactions. Moreover, the highly opened pores of the graphene film allow easy access of the metal salt sources into graphene film, and  $\text{NiCo}_2\text{O}_4$  grew on the surfaces of the graphene sheets to result in the formation of a sandwich-like structure. The hybrid film was finally collected and annealed in air at a temperature of 250  $^{\circ}\text{C}$  for 2 h.

For reliable comparison, the N-doped graphene– $\text{NiCo}_2\text{O}_4$  hybrid film (denoted as NG-NiCo) was prepared similarly by replacing PGO with GO; the porous graphene– $\text{NiCo}_2\text{O}_4$  hybrid film (denoted as PG-NiCo) was obtained following a similar procedure without using  $\text{NH}_3 \cdot \text{H}_2\text{O}$ .

**Characterization.** Powder X-ray diffraction patterns were recorded on a Philips 1130 X-ray diffractometer (40 kV, 25 mA, Cu  $\text{K}\alpha$  radiation,  $\lambda = 1.5418 \text{ \AA}$ ); Fourier transform infrared (FTIR) spectroscopy was recorded on a Nicolet 6700 spectrometer; UV–vis spectroscopy was obtained by using a Shimadzu UV-2600 spectrophotometer; thermogravimetric analysis was conducted on a TGA/SETARAM thermogravimetric analyzer from 100 to 500  $^{\circ}\text{C}$  at a heating rate of 10  $^{\circ}\text{C} \cdot \text{min}^{-1}$  in  $\text{N}_2$  flow; the contact angle was tested on a Theta/Attension optical tensiometer; XPS spectra were recorded on an Axis Ultra (Kratos Analytical, UK). X-ray photoelectron spectroscopy was obtained on an Axis Ultra (Kratos Analytical, UK) XPS spectrometer equipped with an Al Ka source (1486.6 eV); morphologies of the samples were observed on transmission electron microscopy (Tecnai G2 Spirit) and scanning electron microscopy (QUANTA 450); energy-dispersive X-ray spectroscopy was obtained on SEM (QUANTA 450).

MB adsorption experiments were used to probe the accessible surface areas of the samples. Specifically, the samples were put into an MB solution in ethanol (0.1 mg  $\text{mL}^{-1}$ ) and were left at 25  $^{\circ}\text{C}$  for 24 h to allow the accessible surface of the samples to be maximally covered by MB molecules. The amount of adsorbed MB was calculated from the change in the concentration of MB in the solution by UV–vis spectra. The surface area was calculated according to the fact that each milligram of adsorbed MB occupies 2.45  $\text{m}^2$  of surface area.<sup>29,30</sup>

Moreover, the BET surface area and pore volume were evaluated by using nitrogen adsorption–desorption isotherms measured at 77 K on a TriStar II 3020 Micrometrics apparatus. The hybrid film was crushed into fine powder by using a mortar and used for nitrogen adsorption measurement. The BET specific surface area was calculated using adsorption data in a relative pressure range of  $P/P_0 = 0.05–0.3$ . Pore size distribution was derived from the adsorption branch using the BJH method.<sup>27,28</sup> The total pore volume was estimated from the amount adsorbed at a relative pressure ( $P/P_0$ ) of 0.99.

**Electrochemical Measurement.** Electrochemical measurements were performed in a standard three-electrode glass cell on a 760 workstation (Pine Research Instruments, USA) directly using hybrid films as working electrodes, a Pt wire as a counter electrode, and  $\text{Ag}/\text{AgCl}/\text{KCl}$  (3 M) as a reference electrode.

The electrolyte was prepared using Milli-Q water (18 M  $\Omega \text{ cm}^{-1}$ ) and KOH pellets (99.99% weight, Sigma-Aldrich). All measurements were conducted under  $\text{O}_2$  saturation (ultra-high-grade purity, Airgas) to ensure the  $\text{O}_2/\text{H}_2\text{O}$  equilibrium at 1.23 V vs RHE.

Linear scan voltammograms and cyclic voltammetry were conducted with scan rates in the range of 10 to 100 mV  $\text{s}^{-1}$ . Electrical impedance spectroscopy was recorded under the following conditions: ac voltage amplitude 5 mV, frequency ranges  $10^6$  to 1 Hz, and open circuit. Tafel plots were obtained at the scan rate of 10 mV  $\text{s}^{-1}$ . Note that the current density was normalized to the geometrical area and the measured potentials vs  $\text{Ag}/\text{AgCl}$  were converted to a reversible hydrogen electrode (RHE) scale according to the Nernst equation ( $E_{\text{RHE}} = E_{\text{Ag}/\text{AgCl}} + 0.059 \text{ pH} + 0.197$ ); the overpotential ( $\eta$ ) was calculated according to the following formula:  $\eta$  (V) =  $E_{\text{RHE}} - 1.23 \text{ V}$ .

**Conflict of Interest:** The authors declare no competing financial interest.

**Acknowledgment.** This research is financially supported by Australian Research Council (DP1095861, DP130104459).

**Supporting Information Available:** Nitrogen adsorption–desorption isotherm and pore size distribution for  $\text{NiCo}_2\text{O}_4$ ; UV–vis spectra of PNG-NiCo, NG-NiCo, and PNG in MB adsorption experiments; SEM images showing the morphology of  $\text{NiCo}_2\text{O}_4$  and  $\text{NiCo}_2\text{O}_4$  grown on nickel foam; TEM and HRTEM images of PNG-NiCo; SEM elemental mapping of PNG-NiCo; EDS and XPS survey of PNG-NiCo; LSV plots of PNG-NiCo and PG-NiCo; Tafel plots for PNG-NiCo and PG-NiCo; EIS of PNG-NiCo and PG-NiCo; LSV plots of PG-NiCo and NG-NiCo at different scan rates; chronoamperometric response for PNG-NiCo at 0.60 V vs  $\text{Ag}/\text{AgCl}$ ; contact angle of PNG and pristine graphite; zeta distribution of porous graphene; optical image of porous graphene dispersion. This material is available free of charge via the Internet at <http://pubs.acs.org>.

## REFERENCES AND NOTES

- Smith, R. D.; Prevot, M. S.; Fagan, R. D.; Zhang, Z.; Sedach, P. A.; Siu, M. K.; Trudel, S.; Berlinguette, C. P. Photochemical Route for Accessing Amorphous Metal Oxide Materials for Water Oxidation Catalysis. *Science* **2013**, *340*, 60–63.
- Debe, M. K. Electrocatalyst Approaches and Challenges for Automotive Fuel Cells. *Nature* **2012**, *486*, 43–51.
- Chang, Y. H.; Lin, C. T.; Chen, T. Y.; Hsu, C. L.; Lee, Y. H.; Zhang, W.; Wei, K. H.; Li, L. J. Highly Efficient Electrocatalytic Hydrogen Production by  $\text{MoS}_x$  Grown on Graphene-Protected 3D Ni Foams. *Adv. Mater.* **2013**, *25*, 756–760.
- Wang, J.; Zhong, H. X.; Qin, Y. L.; Zhang, X. B. An Efficient Three-Dimensional Oxygen Evolution Electrode. *Angew. Chem., Int. Ed.* **2013**, *52*, 5248–5253.
- Wang, X.; Cao, X.; Bourgeois, L.; Guan, H.; Chen, S.; Zhong, Y.; Tang, D.-M.; Li, H.; Zhai, T.; Li, L.; et al. N-Doped Graphene– $\text{SnO}_2$  Sandwich Paper for High-Performance Lithium-Ion Batteries. *Adv. Funct. Mater.* **2012**, *22*, 2682–2690.
- Yang, X.; Zhu, J.; Qiu, L.; Li, D. Bioinspired Effective Prevention of Restacking in Multilayered Graphene Films: Towards the Next Generation of High-Performance Supercapacitors. *Adv. Mater.* **2011**, *23*, 2833–2888.
- Dikin, D. A.; Stankovich, S.; Zimney, E. J.; Piner, R. D.; Dommett, G. H.; Evmenenko, G.; Nguyen, S. T.; Ruoff, R. S. Preparation and Characterization of Graphene Oxide Paper. *Nature* **2007**, *448*, 457–460.
- Wang, X.; Li, X.; Zhang, L.; Yoon, Y.; Weber, P. K.; Wang, H.; Guo, J.; Dai, H. N-Doping of Graphene through Electro-thermal Reactions with Ammonia. *Science* **2009**, *324*, 768–771.
- Chen, P.; Xiao, T.-Y.; Qian, Y.-H.; Li, S.-S.; Yu, S.-H. Nitrogen-Doped Graphene/Carbon Nanotube Nanocomposite with Synergistically Enhanced Electrochemical Activities. *Adv. Mater.* **2013**, *25*, 3192–3196.
- Stankovich, S.; Dikin, D. A.; Dommett, G. H.; Kohlhaas, K. M.; Zimney, E. J.; Stach, E. A.; Piner, R. D.; Nguyen, S. T.; Ruoff, R. S. Graphene-Based Composite Materials. *Nature* **2006**, *442*, 282–286.

11. Bai, J.; Zhong, X.; Jiang, S.; Huang, Y.; Duan, X. Graphene Nanomesh. *Nat. Nanotechnol.* **2010**, *5*, 190–194.
12. Kotchey, G. P.; Allen, B. L.; Vedala, H.; Yanamala, N.; Kapralov, A. A.; Tyurina, Y. Y.; Klein-Seetharaman, J.; Kagan, V. E.; Star, A. The Enzymatic Oxidation of Graphene Oxide. *ACS Nano* **2011**, *5*, 2098–2108.
13. Zhao, X.; Hayner, C. M.; Kung, M. C.; Kung, H. H. Flexible Holey Graphene Paper Electrodes with Enhanced Rate Capability for Energy Storage Applications. *ACS Nano* **2011**, *5*, 8739–8749.
14. Zhu, Y.; Murali, S.; Stoller, M. D.; Ganesh, K. J.; Cai, W.; Ferreira, P. J.; Pirkle, A.; Wallace, R. M.; Cychosz, K. A.; Thommes, M.; et al. Carbon-Based Supercapacitors Produced by Activation of Graphene. *Science* **2011**, *332*, 1537–1541.
15. Mirzakulova, E.; Khatmullin, R.; Walpita, J.; Corrigan, T.; Vargas-Barbosa, N. M.; Vyas, S.; Oottikkal, S.; Manzer, S. F.; Hadad, C. M.; Glusac, K. D. Electrode-Assisted Catalytic Water Oxidation by a Flavin Derivative. *Nat. Chem.* **2012**, *4*, 794–801.
16. Subbaraman, R.; Tripkovic, D.; Chang, K. C.; Strmcnik, D.; Paulikas, A. P.; Hirunsit, P.; Chan, M.; Greeley, J.; Stamenkovic, V.; Markovic, N. M. Trends in Activity for the Water Electrolyser Reactions on 3d M (Ni, Co, Fe, Mn) Hydr(oxy) Oxide Catalysts. *Nat. Mater.* **2012**, *11*, 550–557.
17. Suntivich, J.; May, K. J.; Gasteiger, H. A.; Goodenough, J. B.; Shao-Horn, Y. A Perovskite Oxide Optimized for Oxygen Evolution Catalysis from Molecular Orbital Principles. *Science* **2011**, *334*, 1383–1385.
18. Trasatti, S. Electrocatalysis in the Anodic Evolution of Oxygen and Chlorine. *Electrochim. Acta* **1984**, *29*, 1503–1512.
19. Ardizzone, S.; Fregonara, G.; Trasatti, S. “Inner” and “Outer” Active Surface of RuO<sub>2</sub> Electrodes. *Electrochim. Acta* **1990**, *35*, 263–267.
20. Gao, M. R.; Xu, Y. F.; Jiang, J.; Zheng, Y. R.; Yu, S. H. Water Oxidation Electrocatalyzed by an Efficient Mn<sub>3</sub>O<sub>4</sub>/CoSe<sub>2</sub> Nanocomposite. *J. Am. Chem. Soc.* **2012**, *134*, 2930–2933.
21. Yin, Q.; Tan, J. M.; Besson, C.; Geletti, Y. V.; Musaev, D. G.; Kuznetsov, A. E.; Luo, Z.; Hardcastle, K. I.; Hill, C. L. A Fast Soluble Carbon-Free Molecular Water Oxidation Catalyst Based on Abundant Metals. *Science* **2010**, *328*, 342–345.
22. Cui, B.; Lin, H.; Li, J.-B.; Li, X.; Yang, J.; Tao, J. Core-Ring Structured NiCo<sub>2</sub>O<sub>4</sub> Nanoplatelets: Synthesis, Characterization, and Electrocatalytic Applications. *Adv. Funct. Mater.* **2008**, *18*, 1440–1447.
23. Li, Y.; Hasin, P.; Wu, Y. Ni<sub>x</sub>Co<sub>3-x</sub>O<sub>4</sub> Nanowire Arrays for Electrocatalytic Oxygen Evolution. *Adv. Mater.* **2010**, *22*, 1926–1929.
24. Liang, Y.; Li, Y.; Wang, H.; Zhou, J.; Wang, J.; Regier, T.; Dai, H. Co<sub>3</sub>O<sub>4</sub> Nanocrystals on Graphene as a Synergistic Catalyst for Oxygen Reduction Reaction. *Nat. Mater.* **2011**, *10*, 780–786.
25. Chen, J.; Sheng, K.; Luo, P.; Li, C.; Shi, G. Graphene Hydrogels Deposited in Nickel Foams for High-Rate Electrochemical Capacitors. *Adv. Mater.* **2012**, *24*, 4569–4573.
26. Wu, Z. S.; Yang, S.; Sun, Y.; Parvez, K.; Feng, X. L.; Mullen, K. 3D Nitrogen-Doped Graphene Aerogel-Supported Fe<sub>3</sub>O<sub>4</sub> Nanoparticles as Efficient Electrocatalysts for the Oxygen Reduction Reaction. *J. Am. Chem. Soc.* **2012**, *134*, 9082–9085.
27. Tillotson, T.; Hrubesh, L. Transparent Ultralow-Density Silica Aerogels Prepared by a Two-Step Sol-Gel Process. *J. Non-Cryst. Solids* **1992**, *145*, 44–50.
28. Kruk, M.; Jaroniec, M.; Sayari, A. Application of Large Pore MCM-41 Molecular Sieves to Improve Pore Size Analysis Using Nitrogen Adsorption Measurements. *Langmuir* **1997**, *13*, 6267–6273.
29. Hang, P. T.; Brindley, G. Methylene Blue Absorption by Clay Minerals. Determination of Surface Areas and Cation Exchange Capacities. *Clays Clay Miner.* **1970**, *18*, 203–212.
30. El-Kady, M. F.; Strong, V.; Dubin, S.; Kaner, R. B. Laser Scribing of High-Performance and Flexible Graphene-Based Electrochemical Capacitors. *Science* **2012**, *335*, 1326–1330.
31. Rasiyah, P.; Tseung, A. A Mechanistic Study of Oxygen Evolution on NiCo<sub>2</sub>O<sub>4</sub> II. Electrochemical Kinetics. *J. Electrochem. Soc.* **1983**, *130*, 2384–2386.
32. Rasiyah, P.; Tseung, A.; Hibbert, D. A Mechanistic Study of Oxygen Evolution on NiCo<sub>2</sub>O<sub>4</sub> I. Formation of Higher Oxides. *J. Electrochem. Soc.* **1982**, *129*, 1724–1727.
33. Hummers, W. S.; Offeman, R. E. Preparation of Graphitic Oxide. *J. Am. Chem. Soc.* **1958**, *80*, 1339–1339.
34. Li, D.; Muller, M. B.; Gilje, S.; Kaner, R. B.; Wallace, G. G. Processable Aqueous Dispersions of Graphene Nanosheets. *Nat. Nanotechnol.* **2008**, *3*, 101–105.